

## Temperature-induced migration of a bubble in a soft microcavity

Bertrand Selva, Isabelle Cantat, and Marie-Caroline Jullien

Citation: *Phys. Fluids* **23**, 052002 (2011); doi: 10.1063/1.3590743

View online: <http://dx.doi.org/10.1063/1.3590743>

View Table of Contents: <http://pof.aip.org/resource/1/PHFLE6/v23/i5>

Published by the [American Institute of Physics](#).

---

### Related Articles

Bubble-driven inertial micropump  
*Phys. Fluids* **24**, 122003 (2012)

Effect of viscosity and shear flow on the nonlinear two fluid interfacial structures  
*Phys. Plasmas* **19**, 122105 (2012)

Bubble nucleation on nano- to micro-size cavities and posts: An experimental validation of classical theory  
*J. Appl. Phys.* **112**, 064904 (2012)

Acoustic-wave effects in violent bubble collapse  
*J. Appl. Phys.* **112**, 054910 (2012)

Critical size of self-propelled motion of droplets on GaAs (100) surface  
*J. Appl. Phys.* **112**, 043523 (2012)

---

### Additional information on Phys. Fluids

Journal Homepage: <http://pof.aip.org/>

Journal Information: [http://pof.aip.org/about/about\\_the\\_journal](http://pof.aip.org/about/about_the_journal)

Top downloads: [http://pof.aip.org/features/most\\_downloaded](http://pof.aip.org/features/most_downloaded)

Information for Authors: <http://pof.aip.org/authors>

### ADVERTISEMENT



**Running in Circles Looking  
for the Best Science Job?**

Search hundreds of exciting  
new jobs each month!

<http://careers.physicstoday.org/jobs>

physicstodayJOBS



## Temperature-induced migration of a bubble in a soft microcavity

Bertrand Selva,<sup>1,2,3</sup> Isabelle Cantat,<sup>4</sup> and Marie-Caroline Jullien<sup>1</sup>

<sup>1</sup>MMN, UMR CNRS 7083, ESPCI ParisTech, F-75231 Paris, France

<sup>2</sup>SATIE, ENS-Cachan, CNRS, UEB, av R. Schuman, F-35170 Bruz, France

<sup>3</sup>UMI 3254, Rhodia Center for Research and Technology, Bristol, Pennsylvania 19007, USA

<sup>4</sup>IPR, UMR CNRS 6251, Université de Rennes 1, F-35000 Rennes, France

(Received 29 March 2011; accepted 19 April 2011; published online 27 May 2011)

We perform studies of pancake-like shaped bubbles submitted to a temperature gradient in a micrometric height Hele-Shaw cell. We show that under the experimental conditions, usually found in microfluidic devices, the temperature-induced dilation of the cavity overcomes the thermocapillary convection due to surface tension variation, effectively driving the bubble toward the cold side of the cavity. The bubble velocity is experimentally characterized as a function of the bubble radius, the temperature gradient, and the initial Hele-Shaw cell thickness. We propose a theoretical prediction of the bubble velocity, based on the analytical resolution of the hydrodynamical problem. The equations set closure is ensured by the pressure value near the bubble and by the dissipation in the moving meniscus. © 2011 American Institute of Physics. [doi:10.1063/1.3590743]

### I. INTRODUCTION

In the future, one may envision microfluidic systems with mazes of microchannels along which droplets conveying solutes, materials or particles would undergo transformations, reactions, and processes. Such systems could be used to perform all sorts of bio/physico-chemical analysis or to produce novel entities. These applications would require the control of elementary operations such as bubble/droplet (further called element) transport, exchange, redirection, and storage. The handling of elements by simple means and at high integration rates then constitutes a key issue.<sup>1</sup> This motivated a number of research groups to develop *digital microfluidics*, a topic entirely dedicated to the manipulation of these elements in microsystems. Prominent examples among available actuators include electro-osmotic<sup>2</sup> and dielectrophoretic solutions.<sup>3</sup> This context has rekindled interest in the Marangoni surface effect, which refers to tangential stresses induced along an interface by a surface tension gradient.<sup>4</sup> Bubbles or droplets can be driven by the flow resulting from such a gradient along their surface. The surface tension at this interface can be tuned by adjusting the local concentration of chemical species or surfactants. This is referred to as *solutocapillarity*.<sup>5–9</sup> The temperature constitutes a second control parameter, and in most systems the surface tension between two fluid phases decreases when the temperature increases. The Marangoni convection induced by a temperature gradient is referred to as *thermocapillarity* or *thermowetting*, whether it involves, respectively, a free surface or a triple contact line.<sup>1,10</sup>

To our knowledge, most of the reported papers in microfluidics focus on droplets wetting at least one wall (thermowetting).<sup>11–15</sup> Thermocapillary effects have mostly been investigated at the macroscopic scale.<sup>10,16–18</sup> In that case, bubbles move toward the high temperature region. This is a consequence of mass conservation around the bubble, as the

continuous phase flows toward the high surface tension (i.e., low temperature) region.<sup>17</sup> In the presence of surfactants, this effect is complicated by a competition with solutocapillarity. The competition between thermocapillary and solutocapillary effects has been first evidenced by Chen and Stebe<sup>19</sup> and then by Brathukin *et al.*<sup>20</sup> They observed a decrease of the traveling bubble velocity (still toward the hot side), a consequence of the accumulation of surfactant at the rear of the bubble. Such competition was also observed in a microfluidic system.<sup>21</sup> According to the experiments conducted by Baroud *et al.*,<sup>21,22</sup> the laser locally induces a reduction in surfactant concentration at the interface along with a local rise in surface tension over the region heated by the laser.

In what follows, we focus on a bubble confined into an elastomeric microcavity, separated from the walls by a thin film of continuous phase, and submitted to a temperature gradient obtained by Joule effect.<sup>23–25</sup> We identify a third physical phenomenon contributing to the droplet motility. The polydimethylsiloxane (PDMS) constituting the cell walls expands when the temperature increases, which results in a cavity thickness gradient. This dilation effect tends to drive the bubbles toward the thickest (i.e., cold) part of the cell, where the curvature radius is the highest.<sup>26–28</sup> This paper discusses quantitatively the competition between this mechanical effect and thermocapillarity. We show that both effects are expected to be of the same order of magnitude. This makes it potentially difficult to predict the element direction of migration in similar geometries, which are commonly used in microfluidics.

In the following section, we describe our experimental set-up, which is similar to Refs. 23 and 24. In Sec. III, we discuss the various physical effects potentially involved in the migration process and estimate their orders of magnitude. Our experimental results are then presented in Sec. IV. We show that the bubble velocity, oriented toward the cold side,

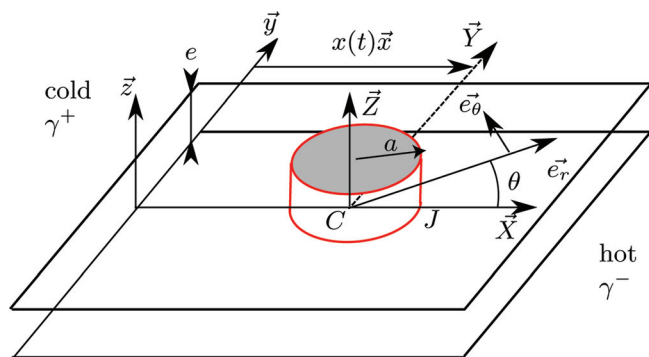


FIG. 1. (Color online) Scheme of the Hele-Shaw cell and notations used in the text.

increases both with bubble radius and temperature gradient, and then it increases when the cell thickness decreases. Section V introduces a theoretical model based on (i) the analysis of the continuous phase flow around the bubble in the observation plane and (ii) the study of the flow in a cross-section of the Hele-Shaw cell, in the vicinity of the bubble interface, which includes the cavity deformation under a temperature gradient (Sec. VI). We eventually compare our numerical and experimental results in Sec. VII.

## II. EXPERIMENTAL SET-UP

### A. System overview and notations

The Hele-Shaw cell is schematically represented in Fig. 1. It is a 2.5 mm long microfluidic cavity of micrometric thickness. The laboratory frame  $\mathcal{R}(0, x, y, z)$  has its origin at the bottom of the cell;  $\vec{z}$  is the normal to the cell, and the temperature gradient is oriented along  $\vec{x}$  and is positive. We only consider bubbles of typical size much larger than the gap  $e$  between the two plates. The bubble is thus squeezed between the plates and adopts a pancake-like shape: in top view, in the  $(\vec{x}, \vec{y})$  plane, it shows as a circle of radius  $a$ ; in the vertical plane  $(\vec{x}, \vec{z})$ , the two menisci are approximated by half circles of radius  $e/2$  (see Fig. 14 for details). The capillary over-pressure in the bubble, of order  $\gamma/e$ , is much larger than the dynamical stresses induced by the motion and the shape remains close to its equilibrium shape. The bubble moves along the  $x$  direction at speed  $U$  ( $U < 0$ ). The bubble centre  $C$  is the origin of the moving frame  $\mathcal{R}_B(C, X, Y, Z)$  and is also the origin of the polar coordinate system  $(C, r, \theta, z)$ . Uppercases are devoted to the study in the  $\mathcal{R}_B$  frame and more precisely in the  $(\vec{X}, \vec{Z})$  plane, whereas lowercases are used in  $\mathcal{R}$ . Finally, tildes correspond to non-dimensional parameters.

### B. Heating device

The experimental set-up is detailed in Refs. 23 and 24. The Hele-Shaw cell is a standard PDMS microfluidic cavity. The temperature gradient is produced by Joule heating from metal resistors etched on a substrate placed below the cavity (cf. Fig. 2). The geometry of the resistor, and more specifically the width of the wires and slits between two adjacent wires, determines the local heat flux injected into the system. In order to generate a constant temperature profile, we coupled two numerical methods to optimize the shape of the resistor: a genetic algorithm<sup>29</sup> and a finite element solver (COMSOL). More detail on this optimization process is given in Ref. 24. As shown in Figure 2, the resistor is composed of five wires in series with decreasing width, leading to an increasing dissipated temperature. They are composed of a 15 nm thick chromium layer and electrically connected by a 150 nm thick gold layer. The Joule effect generated by the gold connexions is negligible compared to the one generated by the chromium layer.

The characterization of the set-up was done using Rhodamine B, a thermally sensitive fluorophore, which fluorescence decreases as the temperature increases.<sup>23,24,30</sup> After calibration, the temperature profile along the cavity can be extracted by image processing, assuming a constant temperature in the  $z$  direction (see paragraph II D).<sup>23</sup> Figure 3(a) displays the measured temperature profiles in the  $x$  direction for four  $y$  values. The four curves collapse on a single straight line, showing that the temperature gradient is constant and oriented along  $x$ . Figure 3(b) shows that this gradient varies linearly with the power supply, consistently with the linearity of the heat conduction problem. The applied power supply varies from  $\mathcal{P} = 65$  to  $\mathcal{P} = 500$  mW and allows us to produce very intense temperature gradients (up to  $11 \text{ K mm}^{-1}$ ) related to  $\mathcal{P}$  by the relation  $\partial T / \partial x = 2.2 \times 10^4 \text{ K m}^{-1} \text{ W}^{-1}$ .

### C. Microfluidic system

A side view of the experimental cell is given in Fig. 2(b). The glass substrate is covered by a thin PDMS membrane (20  $\mu\text{m}$  thick) using a spin-coating technique in order to electrically isolate the resistor. A  $2500 \mu\text{m} \times 1500 \mu\text{m}$  microfluidic cavity, manufactured using classical soft lithography techniques,<sup>31</sup> is sealed to this substrate by oxygen plasma. The height of the cavity is 22  $\mu\text{m}$  or 37  $\mu\text{m}$ .

Bubbles are generated at a T-junction connected to the Hele-Shaw cell by a capillary. A SMC regulator ITV 2030 imposes a gas pressure ranging from 8 to 130 kPa. The flow

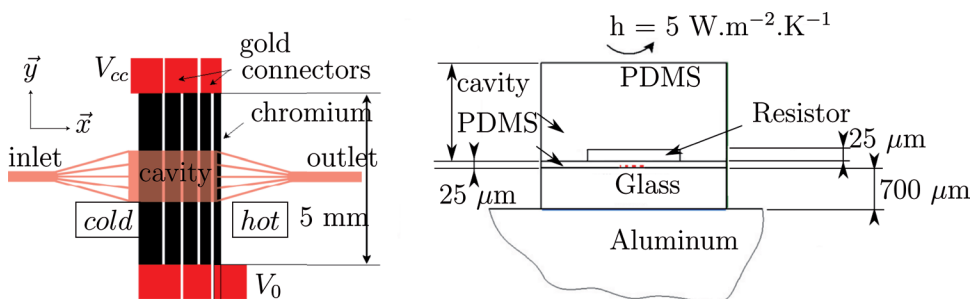


FIG. 2. (a) (Color online) Top view of the heating resistor above which the microfluidic cavity is placed. (b) Side view of the experimental set-up,  $h$  is the thermal exchange coefficient.

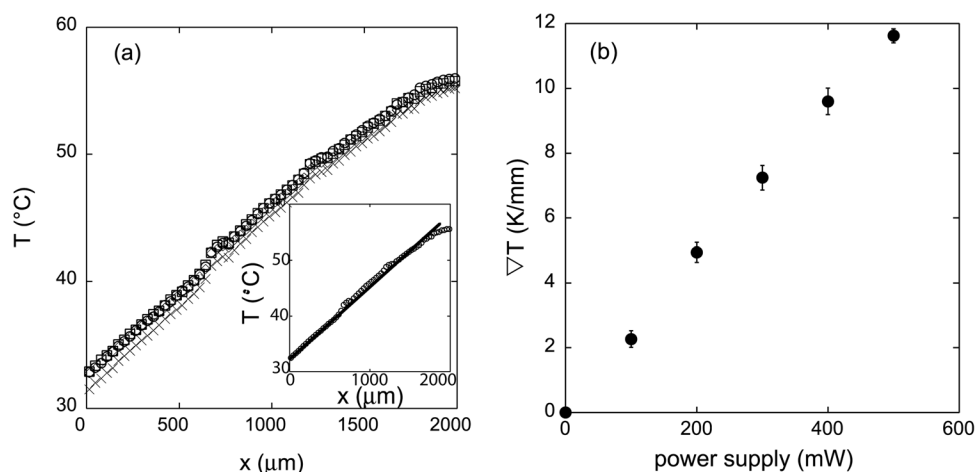


FIG. 3. (a) Experimental temperature profiles along the cavity, for four transverse positions  $y$  and a power supply of 500 mW. The inset shows the mean temperature profile; the standard deviation equals approximately 1% and has consequently not been plotted. (b) Experimental mean temperature gradient along the cavity versus power supply.

rate of the continuous phase is imposed by a syringe pump PHD 2000 (Harvard Apparatus).

The capillary is removed as soon as one bubble reaches the Hele-Shaw cell. We wait for the pressure gradient between the inlet and the outlet to relax and the temperature gradient is imposed when the bubble is at rest in the cavity. The heating power is controlled by the value of the resistance ( $R \sim 2 \text{ k}\Omega$ ) and by the applied voltage which is the tuning parameter.

The continuous phase is deionised water with 5.8% glycerol and sodium dodecyl sulfate (SDS) surfactant at 1.2 cmc (*i.e.*,  $C_0 = 2.7 \text{ g/L} = 0.009 \text{ mol/L}$ ). The dispersed phase is air. For this solution, the surface tension is  $30 \text{ mN m}^{-1}$  at  $35 \text{ }^\circ\text{C}$ . In our temperature range ( $20\text{--}70 \text{ }^\circ\text{C}$ ), we measured a linear surface tension variation<sup>23</sup>  $\partial\gamma/\partial T = -1.85 \times 10^{-4} \text{ N.m}^{-1}.\text{K}^{-1}$ .

#### D. Image recording and processing

In order to visualize the streamlines in the continuous phase while the bubbles are moving, fluorescent particles ( $4.869 \mu\text{m} \pm 0.246 \mu\text{m}$  diameter, Polysciences Inc.) are seeded into the continuous phase. A small amount of fluorescein is also added to the continuous phase in order to extract the contour of the bubble by thresholding the images. We used a Leica MX16 microscope, a video camera COHU 4912, and a set of filters adapted to the fluorescein spectrum. Illumination is provided by a 100 W mercury lamp. Images are processed with the SCION IMAGE software.

The instantaneous bubble velocity, of the order of  $100 \mu\text{m/s}$ , is obtained by measuring the displacement of the geometrical center of the bubble between two successive images. Figure 4 shows a typical bubble velocity as a function of time. After a very short transient, a stationary value is reached. The velocity fluctuations are below 10% during the bubble motion: in the following, we consider only the average of the velocity over the complete trajectory.

### III. OVERVIEW OF THE PHYSICAL PHENOMENA INVOLVED

Several phenomena can induce bubble motility. Tangential stresses at the bubble surface may arise from surface ten-

sion variations, due to an electric field,<sup>32</sup> surfactant concentration,<sup>5,33</sup> or temperature.<sup>10</sup> In addition, mechanical effects such as the dilation of the solution or of the PDMS walls may play a role. In order to discriminate the main phenomena at play, we performed a number of tests, which we now detail.

#### A. Influence of an electrical field

First, we rule out the influence of the electric field due to the presence of the resistor. We estimate its value to  $10^5 \text{ V m}^{-1}$  in the  $x$  direction from the experimental parameters ( $2 \text{ k}\Omega$  resistance,  $0.5 \text{ W}$  heating power, and  $80 \mu\text{m}$  slit width). We built a similar microfluidic device, in which the resistor was replaced by two gold electrodes separated by a distance  $d_e = 3 \text{ mm}$ . This allowed us to generate the same electric field without heating the chamber. We applied AC and DC potentials without witnessing bubble motion.

#### B. Solutocapillary effects

It was necessary to introduce surfactants into the solution in order to avoid dewetting and triple line pinning. These surfactants may contribute to the tangential stress through solutocapillary effects.

The timescale associated with the surfactant binding/unbinding at the interface is much smaller than the typical time scale  $\tau_d = a/u_m \sim 0.2 \text{ s}$  of the experiment, where  $u_m \sim 500 \mu\text{m/s}$  is the maximal liquid velocity near the

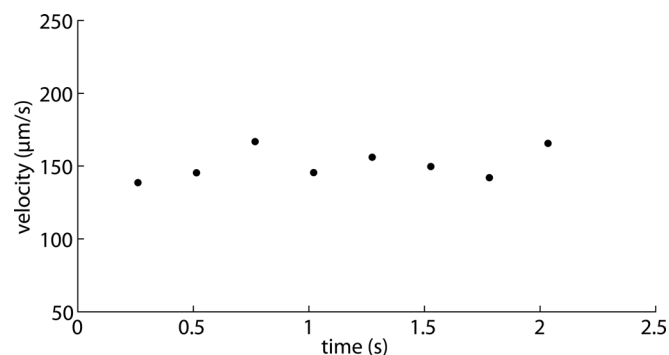


FIG. 4. Instantaneous velocity of a bubble traveling inside the cavity.

interface (at the position  $\theta = \pi/2$ ) and  $a$  is of order  $100 \mu\text{m}$ .<sup>34</sup> The surface concentration is thus at equilibrium with the bulk concentration  $C$  and does not vary as long as  $C$  remains larger than the cmc close to the interface. In the steady state regime, the surfactant fluxes from the surface,  $\Phi_s$ , or from the volume,  $\Phi_v$ , exactly compensate the surfactant advection along the surface  $\Phi_{ad} \sim u_m \Gamma_0/a$  (see Fig. 5). The surface flux,  $\Phi_s \sim D_s \Delta \Gamma/a^2$ , is negligible in comparison with the volume flux,  $\Phi_v \sim D_v \Delta C/\sqrt{D_v \tau_d}$ , where  $D_v$  and  $D_s$  are, respectively, the volume and surface diffusion coefficients of the surfactants,  $\Delta C$  is the bulk concentration variation, and  $\sqrt{D_v \tau_d}$  is the thickness of the diffusive boundary layer, based on the time scale  $\tau_d$ . The mass conservation, at steady state, implies that  $D_v \Delta C/\sqrt{D_v \tau_d} \sim u_m \Gamma_0/a$ . With  $\Gamma_0/C_0 \sim 4 \times 10^{-7} \text{ m}$  (see, for instance, Ref. 35) and  $D_v = 5 \times 10^{-10} \text{ m}^2 \text{ s}^{-1}$ , the ratio  $N_1 = \Delta C/C_0$  can finally be written as

$$N_1 = \frac{\Gamma_0}{C_0} \sqrt{\frac{u_m}{D_v a}} \sim 0.04 \quad (1)$$

This is in agreement with the work of Stebe *et al.*,<sup>36</sup> who proved experimentally, in a different geometry, that the surface remobilisation was obtained for  $N_1 < 0.1$ .

### C. Thermosolutal effects

Another phenomenon may arise from the presence of surfactants in the solution, as their concentration depends on the temperature. The chemical potential in an ideal solution is given by

$$\mu = RT \log(C/C_0). \quad (2)$$

In that ideal case, a temperature gradient induces a bulk concentration gradient in the opposite direction, so that thermocapillarity and the thermosolutal effect have competing influences on the surface tension gradient.

The observation of the streamlines shows that the tangential stress is directed toward the cold region, which means that thermocapillarity dominates, Fig. 7. The thermosolutal contribution thus possibly reduces the magnitude of the thermocapillary convection. A quantitative prediction would require a precise determination of the surfactant chemical potential as a function of the temperature, close to

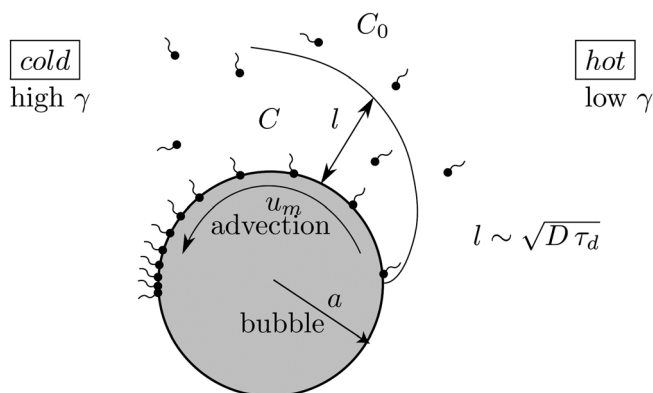


FIG. 5. Schematic of the mechanisms involved in surfactant diffusion and advection along the interface.

the cmc. Note that it does not depend on the size of the bubble [see Eq. (2)].

### D. Vertical thermal diffusion vs. horizontal thermal advection

The thermal regime is also governed by a competition between advection and diffusion. Dimensionally, the diffusion equation in the steady state can be written as

$$u_m \frac{\partial T}{\partial x} \sim D_{th} \frac{\delta T}{e^2},$$

where  $\delta T$  is the temperature variation over the cell thickness and  $D_{th} = 10^{-7} \text{ m}^2 \text{ s}^{-1}$  is the thermal diffusivity. With  $\Delta T$ , the temperature difference along the  $x$  direction over the resistors,  $e = 25 \mu\text{m}$  and  $a/u_m = 0.2 \text{ s}$ , this leads to

$$N_2 = \frac{\delta T}{\Delta T} = \frac{e^2 u_m}{a D_{th}} \sim 0.03. \quad (3)$$

As  $N_2 \ll 1$ , the temperature field is not significantly altered by the flow.

### E. Liquid dilation

Liquid dilation effects may arise from fluxes between regions at different temperatures. We show in Fig. 9 that, in a domain close to the bubble boundary, with a section of order  $e^2$ , the fluid moves at velocity  $u_m \sim 500 \mu\text{m s}^{-1}$  toward the cold regions. A recirculation far from the bubble brings the fluid back to the hot region. The volume occupied by this fluid decreases (or increases) by the amount  $\Delta V/V = \alpha_T \Delta T$ . A flux can be dimensionally built from these quantities,  $Q_{dil} \sim \alpha_T \Delta T e^2 u_m$ . With  $\alpha_T = 2 \times 10^{-4} \text{ K}^{-1}$ , the thermal expansion of water and  $\Delta T \sim 1 \text{ K}$ , the typical temperature difference between both sides of the bubble, we get  $Q_{dil} \sim 6 \times 10^{-17} \text{ m}^3/\text{s}$  to be compared to the volume flux associated to the bubble motion  $Q = a e U \sim 10^{-13} \text{ m}^3/\text{s}$ . We conclude that liquid dilation is not involved in the bubble motion and can be neglected in the model.

### F. PDMS dilation

Contrary to the previously mentioned effects, the PDMS dilation and the associated cell deformation play a crucial role. The temperature field in the whole PDMS block and its thermoelastic response has been computed with the finite element solver COMSOL. The temperature field is determined in the full 3D geometry from the diffusion equation in PDMS and in the liquid phase (at rest, without bubble), with  $\alpha_{T,PDMS} = 3 \times 10^{-4} \text{ K}^{-1}$ , as indicated on the technical data sheet. The induced inhomogeneous dilation leads to elastic stress and deformation. The obtained cell profile is plotted in Fig. 6, in the plane  $y=0$ . The nonmonotonic cell thickness variation results schematically from the competition between (i) PDMS dilation on the side walls, leading to an increase in the cell thickness; (ii) dilation of the PDMS bulk above the cell, which tends to decrease the cell thickness; and (iii) an additional simple shear deformation in the  $-x$  direction. In the middle of the cell, where the bubble migration has been

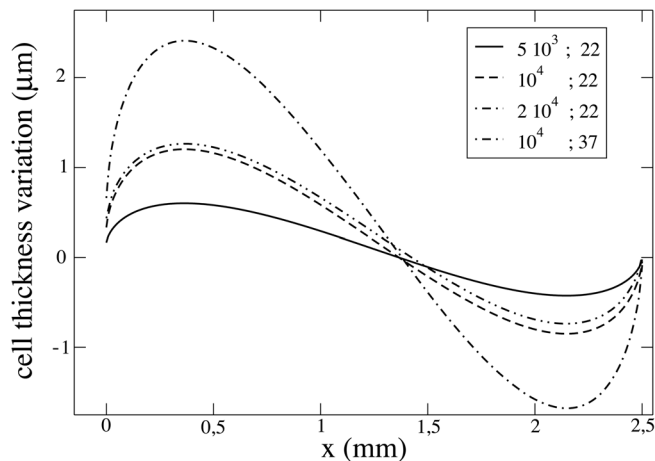


FIG. 6. Cavity roof deformation for different temperature gradients (given in K/m in the legend) and two cell thicknesses (given in  $\mu\text{m}$  in the legend).

recorded, the cell thickness  $e(x)$  is well adjusted by the following law:

$$e(x) = e_0 - 1.7 \times 10^{-7} x \frac{\partial T}{\partial x}. \quad (4)$$

The thickness  $e_0$  is close to the cell thickness at room temperature and does not play any role. For a temperature gradient of 5000 K/m, we thus get a cell thickness difference between both sides of the cell of the order of a micron.

## G. Conclusion

Finally, in light of the previous paragraphs, three main effects can be in competition in the present system: (i) migration induced by a thermocapillary stress, (ii) a thermosolutal contribution which tends to reduce the thermocapillary stress, and (iii) a thermomechanical induced migration. We assume in our model that the surface tension is a function of the temperature only, written as

$$\gamma(x) = \gamma_{eq}(C_0, T(x)) = \gamma_0 + x \frac{\partial \gamma}{\partial x}, \quad (5)$$

where  $\partial \gamma / \partial x$  is constant and depends on the input electrical power. We also take into account the cell thickness variation [Eq. (4)]. In this simplified approach we do not include a potential thermosolutal contribution, which can reduce the magnitude of the thermocapillary effect.

## IV. EXPERIMENTAL RESULTS

In this section, we present the experimental results concerning the displacement of bubbles submitted to a constant temperature gradient in a micrometric Hele-Shaw cell. Bubbles migrate toward the cold side and their velocity increases with the bubble size and the temperature gradient and decreases when the cell thickness increases.

### A. Velocity field in the continuous phase

The streamlines in the continuous phase are represented in the bubble frame in Fig. 7. This figure is obtained from

the superposition of pictures taken over time, after detection and realignment of the geometrical center of the bubble (using the software IMAGEJ).

In the Hele-Shaw cell configuration, the velocity field inside the liquid can be written as  $\vec{v}(x, y, z) = \vec{u}(x, y)w(z)$ , with  $w(z) = 6(z/e - z^2/e^2)$  and  $\vec{u}(x, y)$ , the fluid velocity averaged over the cell thickness (see Sec. IV B).<sup>37</sup> We assume that the tracers are carried at the velocity of the surrounding liquid, so that the velocity of a tracer positioned at an unknown height  $z$  directly yields  $\vec{u}(x, y)$  to within the constant  $w(z)$  ( $0 < w(z) < 1.5$ );  $w(z)$  *a priori* depends on the particle. The superposition of the particle images defines the experimental streamlines, in the bubble reference frame, while the gray scale code gives information on the direction of the flow, i.e., black is the initial time and white is the final time. The main features are (i) a flow faster than the bubble, toward the high surface tension region, on a small domain close to the bubble of typical width  $10 \mu\text{m}$  and (ii) a recirculation toward the low surface tension far from the bubble. The point of velocity cancellation is located at a distance of order  $50 \mu\text{m}$  from the interface. These streamlines are similar to the streamlines observed by Bush in different experimental conditions: a Hele-Shaw cell with a millimetric gap, a bubble submitted to buoyancy, and a tangential stress arising from solutocapillarity.<sup>33</sup>

Among all the tracers visible in Fig. 7, some have been tracked manually. The velocity of tracers from the same position in  $\mathcal{R}_B$  exhibits low fluctuations, which suggest that the tracers stay at the same height. With this assumption, we assume that  $\vec{u}(x, y) = k\vec{v}_p(x, y)$ , where  $k$  is a constant larger than  $1/1.5$  and  $\vec{v}_p$  is the particle velocity. Several tracer velocities are plotted in Figure 8.

The motion of a particle along the bubble boundary ( $r \approx a$  and  $\theta \in [0, \pi]$ , as defined in Fig. 1) is given in Fig. 8. The velocity is oriented along  $u_\theta$  and its amplitude varies like  $\sin \theta$ . We deduce  $\vec{u}_{\mathcal{R}_B}(a, \theta) = u_{m, \mathcal{R}_B} \sin \theta \vec{e}_\theta$ , where  $\vec{u}_{\mathcal{R}_B}$  is the fluid velocity averaged over the cell thickness in the

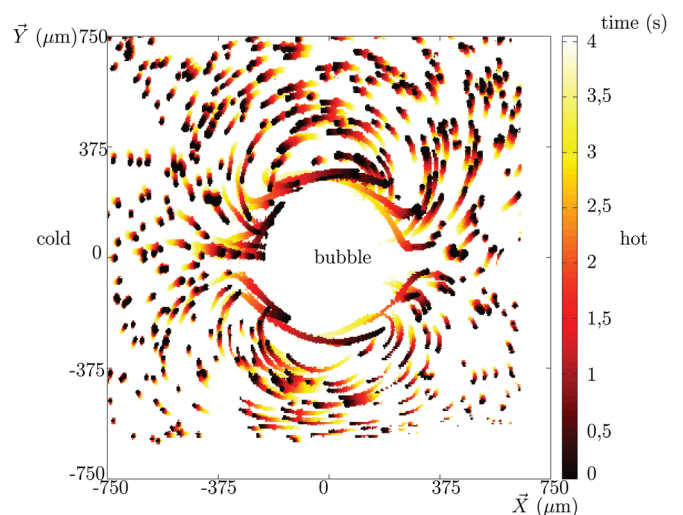


FIG. 7. (Color online) Experimental oriented streamlines in the bubble frame. The image is a superposition of pictures taken with a  $0.05 \text{ s}$  time step. The experimental parameters are:  $a = 230 \mu\text{m}$ ,  $e = 48 \mu\text{m}$ ,  $\partial \gamma / \partial x = -0.21 \text{ Pa}$ , and  $U = -80 \mu\text{m/s}$ .

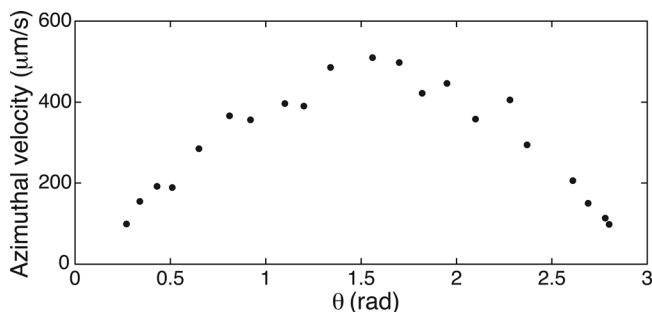


FIG. 8. Instantaneous azimuthal velocity of a particle close to the interface as a function of  $\theta$ , for  $r \approx a$  (same experiment as in Fig. 7).

bubble frame  $\mathcal{R}_B$  and  $u_{m,\mathcal{R}_B} > 0$  is its value at the position  $(a, \pi/2)$ .

Figure 9 presents the azimuthal velocity as a function of  $r$  in the continuous phase for  $\theta = \pi/2$ . As shown in Fig. 7, the azimuthal velocity is positive (oriented toward  $x < 0$ ) for small  $r$  and negative for large  $r$ . Moreover, this figure shows that the velocity gradient close to the boundary verifies  $\partial v_\theta / \partial r (r = a) < 0$ . As the boundary condition for the flow is  $\mu \partial v_\theta / \partial r (r = a) = \partial \gamma / \partial x$  (see Sec. IV C), this provides uncountable experimental evidence that  $\partial \gamma / \partial x < 0$ .

**B. Bubble velocity**

Figure 10 presents the bubble velocity (in absolute value) as a function of the bubble radius for three different temperature gradients and for two different cell thicknesses. The velocity increases with the bubble radius and with the temperature gradient and decreases with the cell thickness.

**V. MODELLISATION: FIRST PART**

In this first part, we determine the flow around the bubble in the laboratory reference frame  $\mathcal{R}$  (see Sec. V A) using classical analytical arguments for Hele-Shaw cells. A second part will be dedicated to solving the pressure field near the bubble, in order to predict the bubble velocity.

**A. Qualitative description of the migration mechanism**

We first give a qualitative analysis of the flow, based on dimensional analysis. The exact solution of the problem will be established in Sec. V B.

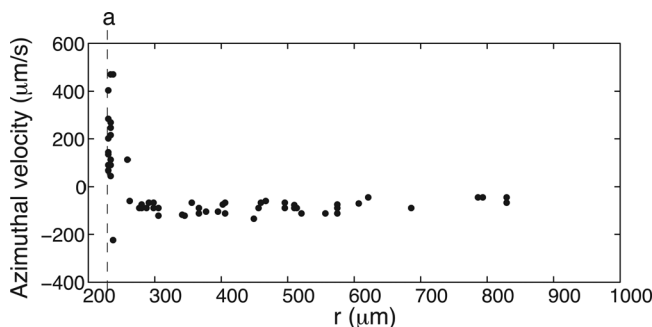


FIG. 9. Instantaneous azimuthal particle velocity as a function of  $r$  for  $\theta = \pi/2$  (same experiment as in Fig. 7).

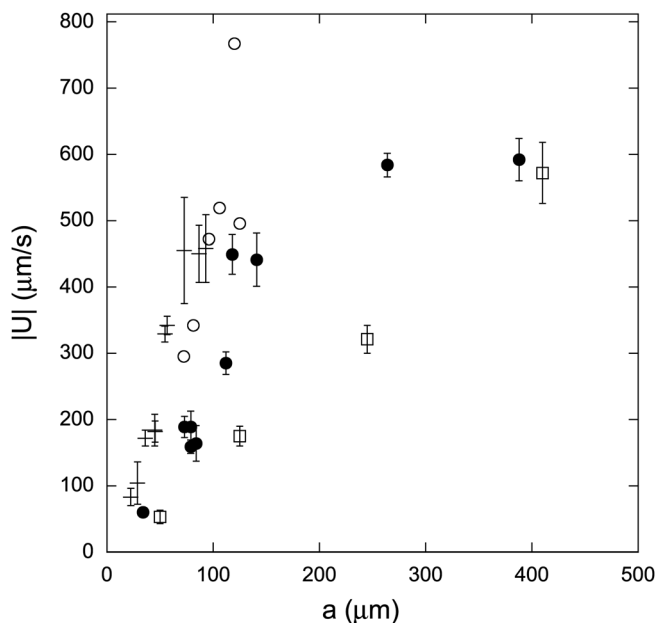


FIG. 10. Bubble velocity  $|U|$  as a function of bubble radius  $a$  for a cell thickness of  $e = 22 \mu\text{m}$  and a power supply of 65 mW ( $\square$ ), 100 mW ( $\bullet$ ), and 200 mW ( $+$ ); and for a cell thickness of  $e = 37 \mu\text{m}$  and a power supply of 300 mW ( $\circ$ ).

Figure 11 is a sketch of the flow areas extracted from the streamlines of Figure 7. The total volume flux across the vertical line in Figure 11 is zero in the laboratory frame. It results from three contributions: the bubble itself, which moves at velocity  $U$ , the flux in zone  $\mathcal{A}$ , where the liquid velocity is high and oriented toward the high surface tension region, and the flux in the recirculation zone  $\mathcal{B}$ . A raw estimation of these three fluxes, disregarding any numerical prefactor, provides the right dimensional expression for the bubble velocity, as a function of the pressure  $p$  around the bubble.

- (1) **Bubble.** The cross-section of the bubble is  $S_{bubble} = a e$ , its velocity is  $U$ , and the flux is  $Q$ .
- (2) **Zone  $\mathcal{A}$ .** The fluid motion is governed by the tangential stress  $\tau \sim \partial \gamma / \partial x$  at the bubble interface. Assuming that

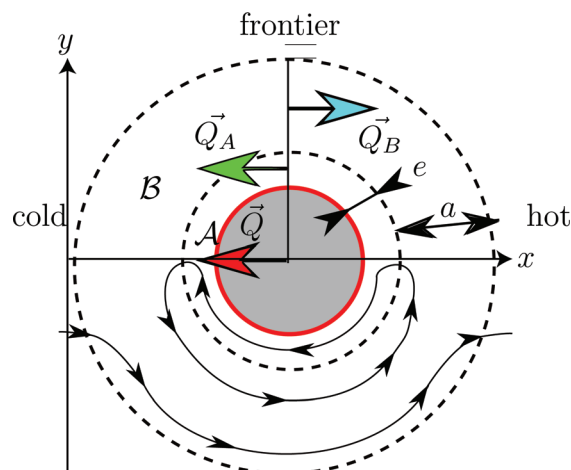


FIG. 11. (Color online) The flows in the continuous phase is split into two zones: zone  $\mathcal{A}$  corresponds to the flow toward the high surface tension region, while zone  $\mathcal{B}$  corresponds to the flow toward the low surface tension region.

the penetration length of this flow in the radial direction scales like the height  $e$  of the moving boundary, we write the stress continuity condition  $\mu u_A/e \sim \partial\gamma/\partial x$ . The section is  $e^2$ , leading to the flux  $Q_A \sim (\partial\gamma/\partial x)(e^3/\mu)$ .

- (3) **Zone B.** Here the fluid moves due to the pressure difference between the front and the rear of the bubble. With  $2\bar{p}(a) = p_{\theta=0,r=a} - p_{\theta=\pi,r=a}$ , the typical velocity in this zone obeys  $\mu u_B/e^2 \sim -\bar{p}(a)/a$ . Assuming the pressure field to be modified by the bubble on a distance of order  $a$ , we get a section  $ae$  and a flux  $Q_B \sim -\bar{p}(a)(e^3/\mu)$ .

The flux balance leads to

$$Uea + \frac{\partial\gamma}{\partial x} \frac{e^3}{\mu} - \frac{\bar{p}(a)e^3}{\mu} = 0 \quad (6)$$

$$U = -\frac{e^2}{\mu a} \left( \frac{\partial\gamma}{\partial x} - \bar{p}(a) \right) \quad (7)$$

In our experiments, both  $\partial\gamma/\partial x$  and  $U$  are negative. Equation (7) therefore implies that  $\bar{p}(a) < 0$ : the bubble moves toward the high pressures. This simple analysis underlines that the bubble velocity strongly depends on  $\bar{p}(a)$ .

Assuming a film curvature equal to  $2/e$  and a cavity deformation due to the thermal gradient, we get an equilibrium Laplace pressure in the fluid  $\bar{p}(a) = \bar{p}_l = -a(\partial/\partial x)(\gamma/e)$ .  $\bar{p}(a) < 0$  implies that the thermomechanical effect overcomes thermocapillarity.

The determination of the pressure is the aim of Sec. VI, and  $\bar{p}(a)$  will be considered as a known parameter in the Sec. VII.

## B. Hele-shaw cell flow hypothesis

We use the classical equations for flows in Hele-Shaw cells,<sup>33,37</sup> based on the assumption that  $e \ll a$ , that the pressure does not depend on  $z$ , and that the velocity field is parallel to the plates and has a parabolic profile along the cell thickness,

$$\vec{u} = \vec{v}(x, y)w(z) \quad (8)$$

with  $w(z) = (6/e^2)(ze - z^2)$ . With this definition, the average velocity over the cell thickness is

$$\langle \vec{u}(x, y, z) \rangle_e = \vec{v}(x, y). \quad (9)$$

The Stokes equation  $\mu\Delta_{3D}\vec{u} = \vec{\nabla}_{3D}p$  simplifies into<sup>37</sup>

$$\vec{\nabla}p = \mu(\Delta\vec{v} - k^2\vec{v}) \quad (10)$$

where  $k = \sqrt{12}/e$  and  $\Delta$  and  $\vec{\nabla}$  denote, respectively, the Laplacian and the gradient in the  $(x, y)$  plane.

The velocity profile is obviously not parabolic close to the bubble boundary. However, this assumption seems to give reliable results,<sup>33,37</sup> even if the systematic derivation of Eq. (10) in power series expansion with  $e/a$  as a small parameter is not clear to us, as discussed in Appendix.

Finally, the mass conservation implies  $\nabla \cdot \vec{v} = 0$ . The cell thickness variation [Eq. (4)] induces a correction of the order of few percent to this relation that is neglected.

This allows us to write the velocity as a function of the stream function  $\psi$

$$\vec{v} = \vec{\text{curl}}(\psi, \vec{z}) \quad (11)$$

and to rewrite Eq. (10) as

$$\Delta(\Delta - k^2)\psi = 0. \quad (12)$$

In the following, we will consider the problem in cylindrical coordinates (see Fig. 1). The velocity field in the continuous phase is given by

$$\begin{cases} v_r &= \frac{1}{r} \frac{\partial\psi}{\partial\theta} \\ v_\theta &= -\frac{\partial\psi}{\partial r} \end{cases}. \quad (13)$$

## C. Boundary conditions

The velocity of the continuous phase in the cavity tends to zero when  $r \rightarrow \infty$ , so that in terms of the stream function

$$\begin{cases} \left( \frac{\partial\psi}{\partial r} \right)_{(r \rightarrow \infty, \theta)} &= 0 \\ \left( \frac{1}{r} \frac{\partial\psi}{\partial\theta} \right)_{(r \rightarrow \infty, \theta)} &= 0 \end{cases} \quad (14)$$

The capillary number is very small (of the order of  $10^{-5}$ ), and we assume that the bubbles keep a circular shape in the  $(\vec{x}, \vec{y})$  plane, as observed on the experimental images. Consistently with Eq. (8), we disregard the interface curvature in the  $(x, z)$  plane and consider the interface shape as a cylinder of radius  $a$  moving at constant velocity  $U$ . The normal velocity in the fluid therefore obeys

$$v_r(r = a) = \left( \frac{1}{a} \frac{\partial\psi}{\partial\theta} \right)_{r=a} = U\vec{x} \cdot \vec{e}_r = U \cos \theta. \quad (15)$$

Finally, there is an equilibrium between the viscous tangential stress and the Marangoni stress  $(\partial\gamma/\partial x) \sin \theta$

$$\sigma_{r\theta}(r = a) = \frac{\partial\gamma}{\partial x} \sin \theta$$

leading to

$$\mu \left( \frac{1}{a^2} \frac{\partial^2\psi}{\partial\theta^2} - \frac{\partial^2\psi}{\partial r^2} + \frac{1}{a} \frac{\partial\psi}{\partial r} \right)_{r=a} = \frac{\partial\gamma}{\partial x} \sin \theta \quad (16)$$

where  $\mu$  is the viscosity of the continuous phase.

The normal stress is given by

$$\sigma_{rr} = -p + 2\mu \frac{\partial v_r}{\partial r} = -p + 2\mu \left( -\frac{1}{r^2} \frac{\partial\psi}{\partial\theta} + \frac{1}{r} \frac{\partial^2\psi}{\partial r \partial\theta} \right). \quad (17)$$

where  $p$  is the pressure field in the continuous phase. Substitution of the solution (to be given in Sec. V E) in this relation will show that the normal stress is dominated by the pressure term.

A normal stress discontinuity arises from the surface tension and interface curvature (the Laplace pressure, see Sec. VI). At this stage, we assume (from symmetry reasons) the  $\theta$  dependency of this discontinuity and we set

$$\begin{aligned} \sigma_{rr}(r=a) &= \left[ -p + 2\mu \left( -\frac{1}{r^2} \frac{\partial \psi}{\partial \theta} + \frac{1}{r} \frac{\partial^2 \psi}{\partial r \partial \theta} \right) \right]_{r=a} \\ &= A_0 + A \cos \theta \end{aligned} \quad (18)$$

Taking the pressure reference  $p_0$  in the fluid phase at the position  $(r=a, \theta=\pi/2)$ , we define

$$p = p_0 + \bar{p}(r) \cos \theta. \quad (19)$$

The unknown parameter  $A$  is thus roughly related to the pressure by the relation  $A \approx -\bar{p}(a)$ .

The pressure field is related to the stream function through the Stokes equation (10), projected along  $\vec{e}_\theta$

$$\begin{aligned} \frac{\partial p}{\partial \theta} &= -\sin \theta \bar{p}(r) \\ &= r\mu \left( -\frac{\partial^3 \psi}{\partial r^3} - \frac{1}{r^2} \frac{\partial^3 \psi}{\partial r \partial \theta^2} - \frac{1}{r} \frac{\partial^2 \psi}{\partial r^2} + \frac{2}{r^3} \frac{\partial^2 \psi}{\partial \theta^2} + \frac{1}{r^2} \frac{\partial \psi}{\partial r} \right) \\ &\quad + \mu k^2 r \frac{\partial \psi}{\partial r} \end{aligned} \quad (20)$$

#### D. Non-dimensional equations

For sake of simplicity, we introduce dimensionless notations  $\psi = \tilde{\psi} U a$ ,  $\Delta = \tilde{\Delta}/a^2$ ,  $r = \tilde{r} a$ ,  $k = \tilde{k}/a$ , the Marangoni number  $M = (a/\mu U)(\partial \gamma/\partial x)$ , and  $A = \tilde{A}(2\mu U/a)$ . Finally, using  $\tilde{\psi} = \varphi \sin \theta$ , Eqs. (12), (15), (16), (18), and (20) are written as a function of  $\tilde{r}$ :

$$\left\{ \begin{array}{l} \tilde{\Delta} (\tilde{\Delta} - \tilde{k}^2) (\varphi \sin \theta) = 0 \\ \varphi(\tilde{r}=1) = 1 \\ \left( -\frac{\partial^2 \varphi}{\partial \tilde{r}^2} + \frac{\partial \varphi}{\partial \tilde{r}} \right)_{\tilde{r}=1} = M + 1 \\ \left( -\frac{\partial^3 \varphi}{\partial \tilde{r}^3} - \frac{\partial^2 \varphi}{\partial \tilde{r}^2} + (4 + \tilde{k}^2) \frac{\partial \varphi}{\partial \tilde{r}} - 4 \right)_{\tilde{r}=1} = 2\tilde{A} \end{array} \right. \quad (21)$$

#### E. Solutions

Boos and Thess<sup>37</sup> solved the partial system, simplified to the first three equations of the complete system (21) by imposing  $M \rightarrow \infty$  (or equivalently  $U=0$ ). They show that this partial system constitutes a closed set of equations with an analytical solution. More generally, we show that these three equations have a solution for any value of  $M$ . As  $M$  is directly related to the bubble velocity, this means that if the normal stress value is not specified, any velocity value is compatible with the boundary conditions. They found the following stream function in the continuous phase

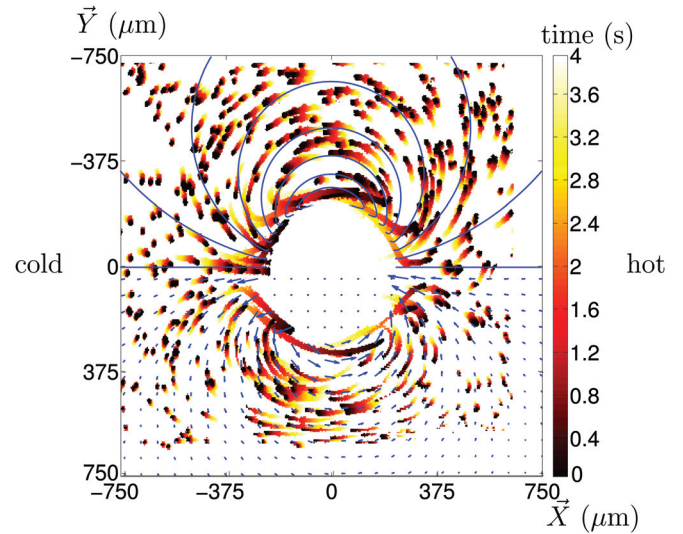


FIG. 12. (Color online) Experimental streamlines within the bubble reference frame for  $a=230 \mu\text{m}$  and  $\partial \gamma/\partial x = -0.21 \text{ Pa}$ , obtained using fluorescent tracers. The solid lines ( $y > 0$ ) and arrows ( $y < 0$ ) on the graph represent the streamlines and velocity vectors given by the stream function given by Eqs. (22)–(24), for the experimental value of  $U$ .

$$\varphi = \frac{C_c}{\tilde{r}} + D_c K_1(\tilde{k}\tilde{r}) \quad (22)$$

where the constants  $C_c$  and  $D_c$  depend on  $M$ .  $K_\nu$  is the modified Bessel function  $K$  of order  $\nu$ .

Figure 12 shows the superposition of the experimental streamlines in the  $(\vec{x}, \vec{y})$  plane and of the theoretical one, deduced from Eq. (22). For this plot,  $C_c$  and  $D_c$  are computed with the value of  $M$  corresponding to the experimental bubble velocity, *i.e.*,

$$C_c = 1 + \frac{K_1(\tilde{k})(M+4)}{\tilde{k}(2K_0(\tilde{k}) + K_1(\tilde{k})\tilde{k})}, \quad (23)$$

$$D_c = -\frac{M+4}{\tilde{k}(2K_0(\tilde{k}) + K_1(\tilde{k})\tilde{k})} \quad (24)$$

Quantitative comparison between theoretical and experimental velocity fields can only be made using an adjustable parameter for  $w(z)$  in Eq. (8), as the tracer position is not known. Figure 13 compares the experimental velocity field (dots) to the field given by Eq. (22) (full line), showing a good agreement with  $w(z) \approx 0.5$ .

Injecting the last equation of the equation set 21, we express the two constants  $C_c$  and  $D_c$  as a function of  $\tilde{A}$  as well as the parameter  $M$

$$M = -\frac{8K_1(\tilde{k})\tilde{k} + 2K_1(\tilde{k})\tilde{k}\tilde{A} + K_1(\tilde{k})\tilde{k}^3 + 4K_0(\tilde{k})\tilde{A} + 2K_0(\tilde{k})\tilde{k}^2}{-2K_0(\tilde{k}) + K_1(\tilde{k})\tilde{k}}. \quad (25)$$

In the limit  $\tilde{k} \rightarrow \infty$ , *i.e.*, for large  $a/e$  values,  $K_\nu(\tilde{k}) \sim e^{-\tilde{k}} \sqrt{\pi/(2\tilde{k})}$ . The asymptotic expression for  $M$  becomes

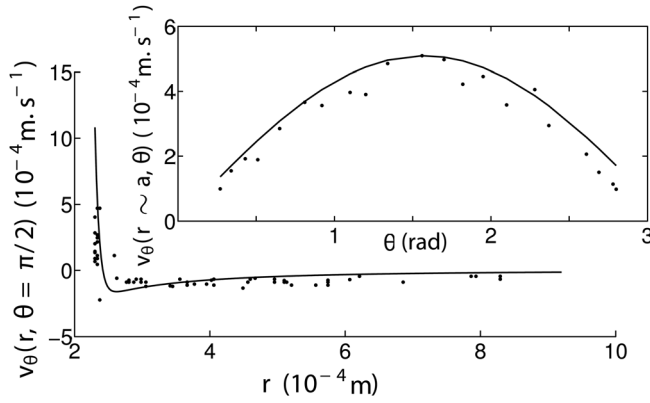


FIG. 13. Tangential velocity  $v_\theta(r, \theta = \pi/2)$  of various tracers in the vicinity of  $\theta = \pi/2$  as a function of radial position  $r$  for  $a = 230 \mu\text{m}$  and  $\partial\gamma/\partial x = -0.21 \text{ Pa}$ . Inset: Tangential velocity  $v_\theta(r, \theta)$  of a single tracer located near the interface as a function of  $\theta$  for the same experiment. Solid lines represent the theoretical values rescaled by an adjustable parameter ( $\sim 0.5$ ).

$$M = \tilde{k}^2 + 2\tilde{A} \quad (26)$$

Equation 25 provides a relation between  $U$  and  $A$ . Its simplified expression [Eq. (26)] is, in dimensioned variables

$$U = -\frac{e^2}{a\mu} \left( \frac{1}{2} \frac{\partial\gamma}{\partial x} + \frac{A}{6} \right). \quad (27)$$

This expression, valid for large bubbles, confirms our qualitative analysis from Sec. V A [using  $A \approx -\bar{p}(a)$  in Eq. (7)].

## VI. MODELISATION: SECOND PART

This second part of the modeling deals with the determination of the pressure field at the bubble boundary or equivalently of the parameter  $A$ .

### A. SHAPE OF THE BUBBLE OUT OF EQUILIBRIUM

#### 1. Shape of the interface at equilibrium and Laplace pressure

Without temperature gradient, the bubble has an axisymmetric pancake-like shape as depicted in Fig. 14. The curved sides of its cross-section is well approximated by a hemi-ellipse (dotted line in Fig. 14) of axis  $e$  and  $b = e(1 - e/(6a))$

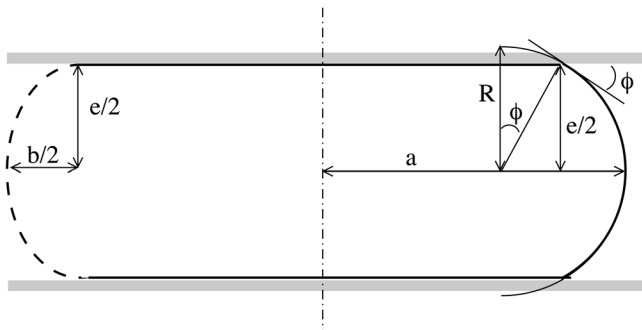


FIG. 14. Schematic view of the bubble cross-section. The lateral boundary of the cross-section  $\mathcal{L}$  (in dotted line on the picture) is close to a hemi circle of radius  $e/2$ . Two corrections, discussed in the text, are illustrated here. Left side: a small curvature variation along  $\mathcal{L}$  arising from the finite value of the bubble radius  $a$ . Right side: a non-zero contact angle arising from the disjoining pressure contribution.

determined from the constant mean curvature constraint at first order in  $e/a$ .<sup>38</sup> With a mean curvature of  $(2/e)(1 + e/(3a))$ , the Laplace pressure at equilibrium is

$$p_l = -\gamma \frac{2}{e} \left( 1 + \frac{e}{3a} \right). \quad (28)$$

The continuous phase wets the PDMS so that a thin film separates the bubble and the PDMS. However, the surface tension depends on the film thickness and its value,  $\gamma_f$ , may be slightly smaller in the wetting film than at the free liquid/gas interface. This leads to an angle discontinuity  $\phi$  along the contact line separating the wetting film and the free interface (seen at a macroscopic scale).<sup>39</sup> This angle  $\phi$  satisfies  $\cos \phi = \gamma_f/\gamma$ , so  $\phi \sim \sqrt{2(\gamma - \gamma_f)/\gamma}$  and is the order of a few degrees or less. As discussed in the next paragraph, a non-zero contact angle also arises from dynamical reasons. The radius of curvature  $R$  in the film (in the  $(x,z)$  plane) verifies  $R \cos \phi = e/2$  (see Fig. 14). At leading order in  $\phi$  this leads to

$$p_l = -\gamma \frac{2}{e} \left( 1 + \frac{e}{3a} - \frac{\phi^2}{2} \right). \quad (29)$$

#### 2. Bretherton's law and Tanner's law

The motion of the bubble induces interface deformations and a dynamical variation of the Laplace pressure, due to the viscous forces in the meniscus. The classical Bretherton's law<sup>40,41</sup> predicts

$$p_l = -\gamma \frac{2}{e} \left( 1 + \alpha_B (\eta|U|/\gamma)^{2/3} \right) \quad (30)$$

with  $\alpha_B = 3.8$  at the front of the bubble ( $x = -a$ ) and  $\alpha_B = -1.9$  at the rear of the bubble ( $x = a$ ).

However, the thickness of the wetting film trapped between the static wall and the moving bubble predicted by the same theory is  $H_{dyn} \approx R(\eta U/\gamma)^{2/3}$ , with  $R$  the radius of curvature of the interface at the front of the bubble (here  $R = e/2$ ).<sup>40,42,43</sup> In our geometry, this relation leads to the order of magnitude  $H_{dyn} \approx 2 \text{ nm}$ , which is probably lower than the equilibrium thickness  $H_{eq}$ . The disjoining pressure is thus non-negligible, even in the dynamical regime.

In that case, the Tanner's law applies. It relies on the same physical assumptions, but takes into account a cut off at the microscopic scale<sup>44,45</sup> and predicts a dynamical contact angle  $\phi^3 \approx 9(\eta U/\gamma) \ln(\ell_{macro}/\ell_{micro})$  at the rear of the bubble. Neglecting  $e/a$  in Eq. (29) and injecting the out of equilibrium macroscopic contact angle  $\phi$  leads to (for  $U < 0$ )

$$p_{l, rear} = -\gamma \frac{2}{e} \left( 1 + \alpha_T (\eta|U|/\gamma)^{2/3} \right) \quad (31)$$

with  $\alpha_T = (9 \ln(\ell_{macro}/\ell_{micro}))^{2/3}/2$ . Using  $\ell_{macro} = e = 20 \mu\text{m}$  and  $\ell_{micro} = H_{eq} \approx 20 \text{ nm}$ , we get  $\alpha_T = 8$ , of the same order as  $\alpha_B$ . To our knowledge, the pressure drop at the front meniscus has not been predicted in the confined case.

These two models are very similar and both lead to the relation

$$p_l = -\gamma \frac{2}{e} \left( 1 \pm \alpha (\eta |U| / \gamma)^{2/3} \right) \quad (32)$$

where  $\alpha$  is a numerical prefactor of order 5. The sign is positive at the front of the bubble and negative at the rear of the bubble.

Finally, the normal stress difference between both sides of the bubble is well approximated by

$$A = \frac{\partial \gamma}{\partial x} \frac{2a}{e} - \frac{2a\gamma}{e^2} \frac{\partial e}{\partial x} + \frac{U}{|U|} \frac{2\gamma\alpha}{e} \left( \frac{\eta |U|}{\gamma} \right)^{2/3}. \quad (33)$$

The three terms are *a priori* of the same order, 10 Pa. However, we saw in Sec. VI A that  $U < 0$  imposes  $A > 0$ , which implies that in this case the second term overcomes the two others: in our experiments, the dilation effect dominates.

## VII. PREDICTIONS OF THE MODEL AND COMPARISON WITH EXPERIMENTS

### A. Theoretical bubble velocity

In the light of the Sec. V and VI, we can now predict the bubble velocity as a function of the temperature gradient, bubble radius, and cell thickness. Equations (26) (valid in the limit  $a \gg e$ ) and (33) lead to

$$\frac{a\mu}{e^2} U + \frac{U}{|U|} \frac{\gamma\alpha}{3e} \left( \frac{\eta |U|}{\gamma} \right)^{2/3} + \frac{\partial \gamma}{\partial x} \left( \frac{1}{2} + \frac{a}{3e} \right) - \frac{a\gamma}{3e^2} \frac{\partial e}{\partial x} = 0. \quad (34)$$

With  $a = [50 - 200] \mu\text{m}$  and  $U = [50 - 500] \mu\text{m/s}$ , we have  $a\mu U / e^2 \ll (4\gamma\alpha/e)(\eta |U|/\gamma)^{2/3}$ , which leads to

$$\frac{U}{|U|} \left( \frac{\eta |U|}{\gamma} \right)^{2/3} = \frac{a}{\alpha} \left( \frac{1}{e} \frac{\partial e}{\partial x} - \frac{1}{\gamma} \frac{\partial \gamma}{\partial x} \right). \quad (35)$$

If  $U < 0$ , we get

$$|U| = \left| \frac{\gamma}{\eta} \left( \frac{a}{\alpha} \right)^{3/2} \left( \frac{1}{e} \frac{\partial e}{\partial x} - \frac{1}{\gamma} \frac{\partial \gamma}{\partial x} \right)^{3/2} \right|. \quad (36)$$

### B. Comparison between the experiment and the model

Equation (35) fully predicts the velocity, with no adjustable parameter. As detailed above, the direction of migration of the bubbles toward the cold side is a signature of the predominance of thermomechanical effects over the thermocapillary ones, i.e.,  $(1/\gamma)|\partial\gamma/\partial x| < (1/e)|\partial e/\partial x|$  (see Fig. 15). To go beyond this qualitative agreement, Fig. 16 shows the best adjustment for our experimental data by

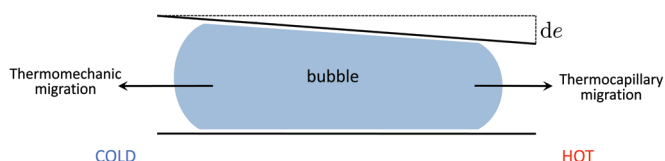


FIG. 15. (Color online) Sketch of the competition between thermocapillary and thermomechanical effects on bubble migration.

$$\left( \frac{\eta |U|}{\gamma} \right)^{2/3} = \frac{a}{\alpha e} \beta \frac{\partial T}{\partial x} \quad (37)$$

where  $\alpha = 4.83$  is the only adjustable parameter, very close to the theoretical value 5.  $\beta = 1.7 \times 10^{-7}$  is given by our COMSOL calculations for  $\partial e/\partial x$ , relation (4): here, we assume that  $(1/\gamma)|\partial\gamma/\partial x| \ll (1/e)|\partial e/\partial x|$ . The quantitative agreement between our model and the experimental data, up to radii of about  $200 \mu\text{m}$ , further confirms that the dilation effect dominates in our experiments.

However, a rough estimation of the thermocapillary contribution in our set-up gives the same order of magnitude than the thermomechanical contribution.

This indicates that we overestimate  $(1/\gamma)|\partial\gamma/\partial x|$ . As mentioned in Sec. C, we believe this is due to the thermosolutal contribution that can lead to a reduction of the effective surface tension gradient.

In the inset of Figure 16, the discrepancy for bubble radii larger than  $200 \mu\text{m}$  arises from side effects of the Hele-Shaw cell. Indeed, the amplitude of the recirculations around the bubble reaches the size of the cavity for such large radii (see mass balance in Figure 11).

## VIII. CONCLUSION

In this paper, we investigate the migration of a bubble in a soft microcavity exposed to a constant temperature gradient. To do so, we combined microfluidic experiments, COMSOL simulations, and a theoretical model. We identify three competing mechanisms that arise from the temperature gradient: (i) thermocapillarity, which tends to drive the bubble toward the hot side, opposing; (ii) a mechanical effect due to the variation in cavity thickness; and (iii) a thermosolutal contribution arising from fluctuations in the surfactant concentration. A theoretical

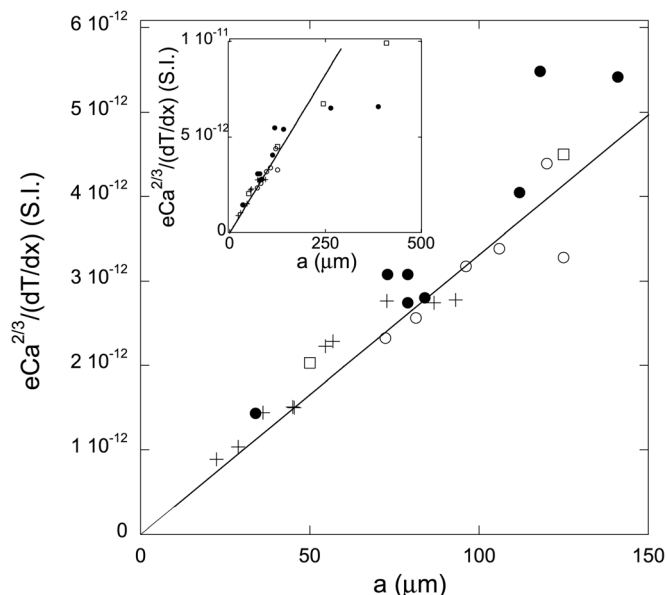


FIG. 16.  $eCa^{2/3}/(\partial T/\partial x)$  as a function of the bubble radius  $a$  ( $a < 150 \mu\text{m}$ ), for a cell thickness of  $e = 22 \mu\text{m}$  and a power supply of 65 mW ( $\square$ ), 100 mW ( $\bullet$ ), and 200 mW ( $+$ ); and for a cell thickness of  $e = 37 \mu\text{m}$  and a power supply of 300 mW ( $\circ$ ). Straight line: theoretical prediction for  $\alpha = 4.83$  [Eq. (37)]. Inset: same results for all values of  $a$ .

model, which does not take thermosolutal effects into account, yields predictions in quantitative agreement with our experimental data, indicating the cavity dilation to be the dominant effect. We believe this study to be of practical interest to the field of digital microfluidics, as promising technologies rely on droplet-based applications in temperature-controlled microfluidic systems.<sup>46–48</sup>

## ACKNOWLEDGMENTS

The authors would like to thank H. A. Stone for his valuable suggestion to take into account dilation effects and D. Quéré for fruitful discussions. The authors are also grateful to Nais Coq for her input. The authors also wish to thank CNRS, ENS-Cachan, ESPCI, and Université de Rennes 1 for fundings. Finally IC acknowledges an IUF grant.

## APPENDIX: HELE-SHAW EQUATIONS

The aim of this Appendix is to establish Eq. (10), starting from the Stokes equation  $\mu\Delta_{3D}\vec{u} = \vec{\nabla}_{3D}p$ , in the Hele-Shaw approximation, *i.e.*, using  $\varepsilon = e/a$  as a small parameter. We rescale the spatial variables  $x$ ,  $y$ , and  $z$ , respectively, by  $a$ ,  $a$ , and  $e$  and the velocity component  $u_x$ ,  $u_y$ , and  $u_z$ , respectively, by  $U$ ,  $U$ , and  $\varepsilon U$ . The pressure  $p$  is rescaled by  $\mu U/(ae^2)$ .

The Stokes equations becomes, with the same notations for the adimensioned variables

$$\partial_x u_x + \partial_y u_y + \partial_z u_z = 0 \quad (\text{A1})$$

$$\varepsilon^2 \partial_{xx} u_x + \varepsilon^2 \partial_{yy} u_x + \partial_{zz} u_x = \partial_x p \quad (\text{A2})$$

$$\varepsilon^2 \partial_{xx} u_y + \varepsilon^2 \partial_{yy} u_y + \partial_{zz} u_y = \partial_y p \quad (\text{A3})$$

$$\varepsilon^4 \partial_{xx} u_z + \varepsilon^4 \partial_{yy} u_z + \varepsilon^2 \partial_{zz} u_z = \partial_z p. \quad (\text{A4})$$

Expanding  $u_x$ ,  $u_y$ ,  $u_z$ , and  $p$  in power series in  $\varepsilon$ , with the notation  $u = u_0 + \varepsilon u_1 + \varepsilon^2 u_2 + \dots$  we get at order 0 and 1 the usual relations

$$\begin{aligned} \partial_z p_0 &= 0 & \partial_{zz} u_{x,0} &= \partial_x p_0 & \partial_{zz} u_{y,0} &= \partial_y p_0, \\ \partial_z p_1 &= 0 & \partial_{zz} u_{x,1} &= \partial_x p_1 & \partial_{zz} u_{y,1} &= \partial_y p_1. \end{aligned}$$

Up to the first order 1, the velocity profile is parabolic, because  $p$  does not depend on  $z$ .

At order 2, we get

$$\begin{aligned} \partial_z p_2 &= \partial_{zz} u_{z,0} & \partial_{zz} u_{x,2} + \Delta u_{x,0} &= \partial_x p_2 \\ \partial_{zz} u_{y,2} + \Delta u_{y,0} &= \partial_y p_2. \end{aligned}$$

The 2D Laplacian appears in the Stokes equation at this order, as written in Eq. 10. However, profile of the velocity is no longer parabolic as  $\partial_z p_2$  becomes non-negligible. Corrections of same order as  $\Delta \vec{u}_0$  may arise from  $\partial_{zz} \vec{u}_2$ . Considering these corrections would imply to deal with the full 3D problem.

<sup>1</sup>T. M. Squires and S. R. Quake, “Microfluidics: Fluid physics at the nanoliter scale,” *Rev. Mod. Phys.* **77**, 977 (2005).

<sup>2</sup>P. S. Dittich and P. Schwillie, “An Integrated microfluidic system for reaction, high-sensitivity detection, and sorting of fluorescent cells and particles,” *Anal. Chem.* **75**(21), 5767 (2003).

- <sup>3</sup>K. Ahn, C. Kerbage, T. P. Hunt, and R. M. Westervelt, “Dielectrophoretic manipulation of drops for high-speed microfluidic sorting devices,” *Appl. Phys. Lett.* **88**(2), 024104 (2006).
- <sup>4</sup>S. H. Davis, “Thermocapillary instabilities,” *Ann. Rev. Fluid Mech.* **19**, 403 (1987).
- <sup>5</sup>V. G. Levich, *Physicochemical Hydrodynamics* (Prentice-Hall, Englewood Cliffs, NJ, 1962).
- <sup>6</sup>V. G. Levich and A. M. Kuznetsov, “Droplet motions in liquids caused by surface active substances,” *Dokl. Akad. Nauk SSSR*, **146**, 145 (1962).
- <sup>7</sup>V. G. Levich and V. S. Krylov, “Surface tension driven phenomena,” *Annu. Rev. Fluid Mech.* **1**, 293 (1969).
- <sup>8</sup>C. D. Eggleston, Y. P. Pawar, and K. J. Stebe, “Insoluble surfactants on a drop in an extensional flow: A generalization of the stagnated surface limit to deforming interfaces,” *J. Fluid Mech.* **385**, 79 (1999).
- <sup>9</sup>R. Hanumanthu and K. J. Stebe, “Transient enhancement of thermocapillary flow in two-dimensional cavity by a surfactant,” *Phys. Fluids* **19**, 042103 (2007).
- <sup>10</sup>N. O. Young, J. S. Golstein, and M. J. Block, “The motion of bubbles in a vertical temperature gradient,” *J. Fluid Mech.* **6**, 350 (1959).
- <sup>11</sup>Z. Jiao, N.-T. Nguyen, and X. Huang, “Reciprocating thermocapillary plug motion in an externally heated capillary,” *AIChE J.* **45**(2), 350 (2007).
- <sup>12</sup>N.-T. Nguyen and X. Huang, “Thermocapillary effect of a liquid plug in transient temperature fields,” *Jpn. J. Appl. Phys.* **44**, 1139 (2005).
- <sup>13</sup>A. A. Darhuber, J. P. Valentino, J. M. Davis, and S. M. Troian, “Microfluidic actuation by modulation of surface stresses,” *Appl. Phys. Lett.* **82**, 657 (2003).
- <sup>14</sup>A. A. Darhuber, J. P. Valentino, S. M. Troian and S. Wagner, “Thermocapillary actuation of droplets on chemically patterned surfaces by programmable microheater arrays,” *J. Microelectromech. Syst.* **12**, 873 (2003).
- <sup>15</sup>Z. Jiao, X. Huang, and N.-T. Nguyen, “Thermocapillary actuation of droplet in a planar microchannel,” *Microfluid. Nanofluid.* **5**, 205 (2008).
- <sup>16</sup>Y. K. Bratukhin and A. L. Zuev, “Thermocapillary drift of an air bubble in a horizontal Hele-Shaw cell,” *Fluid Dyn.* **19**(3), 393 (1984).
- <sup>17</sup>E. Lajeunesse and G. M. Homsy, “Thermocapillary migration of long bubbles in polygonal tubes. II. Experiments,” *Phys. Fluids*, **15**, 308 (2003).
- <sup>18</sup>A. Mazouchi and G. M. Homsy, “Thermocapillary migration of long bubbles in polygonal tubes. I. Theory,” *Phys. Fluids*, **13**, 1594 (2001).
- <sup>19</sup>J. Chen and K. J. Stebe, “Surfactant-induced retardation of the thermocapillary migration of droplet,” *J. Fluid. Mech.* **340**, 35 (1997).
- <sup>20</sup>Y. K. Bratukhin, K. G. Kostarev, A. Viviani, and A. L. Zuev, “Experimental study of Marangoni bubble migration in normal gravity,” *Exp. Fluids*, **38**, 594 (2005).
- <sup>21</sup>E. Vermeuil, M. Cordero, C. N. Baroud, and E. de Langre, “Laser-induced force on a microfluidic drop: Origin and magnitude,” *Langmuir* **25**, 5127 (2009).
- <sup>22</sup>C. N. Baroud, J.-P. Delville, F. Gallaire, and R. Wunenburger, “Thermocapillary valve for droplet production and sorting,” *Phys. Rev. E.* **75**, 4 (2007).
- <sup>23</sup>B. Selva, J. Marchalot, and M.-C. Jullien, “An optimized resistor pattern for temperature gradient control in microfluidics,” *J. Micromech. Microeng.* **19**, 065002 (2009).
- <sup>24</sup>B. Selva, P. Mary, and M.-C. Jullien, “Integration of a uniform and rapid heating source into microfluidic systems, *Microfluid. Nanofluid.* **8**, 755 (2010).
- <sup>25</sup>B. Selva, V. Miralles, I. Cantat, and M.-C. Jullien, “Thermocapillary actuation by optimized resistor pattern: Bubbles and droplets displacing, switching and trapping,” *Lab Chip* **10**, 1835 (2010).
- <sup>26</sup>E. Lorenceau and D. Quéré, “Drops on a conical wire,” *J. Fluid Mech.* **510**, 29 (2004).
- <sup>27</sup>P. Renvoisé, J. W. M. Bush, M. Prakash, and D. Quéré, “Drop propulsion in tapered tubes,” *Euro. Phys. Lett.* **86**, 64003 (2009).
- <sup>28</sup>R. Dangla, F. Gallaire, and C. N. Baroud, “Microchannel deformations due to solvent-induced PDMS swelling,” *Lab Chip* **10**, 2032 (2010).
- <sup>29</sup>K. Deb, *Multi-Objective Optimization Using Evolutionary Algorithms* (John Wiley and Sons, Chichester, UK, 2001), ISBN 0-471-87339-X.
- <sup>30</sup>D. Ross, M. Gaitan, and L. E. Locascio, “Temperature measurement in microfluidic systems using a temperature-dependent fluorescent dye,” *Anal. Chem.* **73**, 4117 (2001).
- <sup>31</sup>Y. Xia and G. M. Whitesides, “Soft Lithography,” *Annu. Rev. Mater. Sci.* **28**, 153 (1998).
- <sup>32</sup>J. S. Newman, *Electrochemical Systems* (Prentice-Hall, Englewood Cliffs, NJ, 1991).
- <sup>33</sup>J. W. M. Bush, “The anomalous wake accompanying bubbles rising in a thin gap: A mechanically forced Marangoni flow,” *J. Fluid Mech.* **352**, 283 (1997).

- <sup>34</sup>D. Quéré and A. de Ryck, "Le mouillage dynamique des fibres," *Ann. Phys. Fr.* **23**, 1 (1998).
- <sup>35</sup>C. H. Chang and E. I. Franses, "Adsorption dynamics of surfactants at the air/water interface: A critical review of mathematical models, data, and mechanism," *Colloids. Surf. A.* **100**, 1 (1995).
- <sup>36</sup>K. J. Stebe, S.-Y. Lin, and C. Maldarelli, "Remobilizing surfactant retarded fluid particle interfaces. I. Stress-free conditions at the interfaces of micellar solutions of surfactants with fast sorption kinetics," *Phys. Fluids A* **3**, 3 (1991).
- <sup>37</sup>W. Boos and A. Thess, "Thermocapillary flow in a Hele-Shaw cell," *J. Fluid Mech.* **352**, 305 (1997).
- <sup>38</sup>C. Gay, P. Rognon, D. Reinelt, and F. Molino, "Rapid Plateau border size variations expected in three simple experiments on 2D liquid foams," *Euro. Phys. J. E* **34**, 110023 (2011).
- <sup>39</sup>A. V. Neimark and "M. Vignes-Adler Variations from the Plateau law in foams," *Phys. Rev. E* **51**, 788 (1995).
- <sup>40</sup>F. P. Bretherton, "The motion of long bubbles in tubes," *J. Fluid Mech.* **10**, 166 (1961).
- <sup>41</sup>A. R. Kopf-Sill and G. M. Homsy, "Bubble motion in a Hele Shaw cell," *Phys. Fluids A* **31**, 18 (1987).
- <sup>42</sup>L. Landau and V. Levich, "Dragging of a liquid by a moving plate," *Acta Physicochim. URSS* **17**, 42 (1942).
- <sup>43</sup>R. Krechetnikov and G. M. Homsy, "Surfactant effects in the landau-levich problem," *J. Fluid Mech.* **559**, 429 (2006).
- <sup>44</sup>P. G. de Gennes, "Wetting: Statics and dynamics," *Rev. Mod. Phys.* **57**, 827 (1985).
- <sup>45</sup>J. Eggers and H. A. Stone, "Characteristic lengths at moving contact lines for a perfectly wetting fluid: The influence of speed on the dynamic contact angle," *J. Fluid Mech.* **505**, 309 (2004).
- <sup>46</sup>S. Koster, F. E. Angile, H. Duan, J. J. Agresti, A. Wintner, C. Schmitz, A. C. Rowat, C. A. Merten, D. Pisignano, A. D. Griffith, and D. A. Weitz, "Drop-based microfluidic devices for encapsulation of single cells," *Lab Chip* **8**, 1110 (2008).
- <sup>47</sup>M. M. Kiss, L. Ortoleva-Donnelly, N. R. Beer, J. Warner, C. G. Bailey, B. W. Colston, J. M. Rothberg, D. R. Link, and J. H. Leamon, "High-throughput quantitative polymerase chain reaction in picoliter droplets," *Anal. Chem.* **80**, 8975 (2008).
- <sup>48</sup>U. Lehman, C. Vandevyver, V. K. Parashar, and M. A. M. Gijs, "Droplet-based DNA purification in a magnetic lab-on-a-chip," *Angew. Chem., Int. Ed.* **45**, 3062 (2006).